Numerical Study of Plasma Density Gradient Effects on Farley-Buneman Waves Traveling in the Equatorial E Region

Chi-Lon Fern[1, *] and Fu-Shong Kuo [2]

[1] Graduate School of Materials Science, National Yunlin University of Science and Technology, Douliou, Yunlin, Taiwan, ROC
[2] Department of Electro-Optical Engineering, Van Nung University, Chung-Li, Taiwan, ROC

ABSTRACT

In this paper, a two-dimensional numerical study of a plasma density gradient effect on Farley-Buneman waves (FB waves) is performed via a two-fluid code in which the electron inertia is neglected while the ion inertia is retained. We focused the simulations on the interaction between a single wave mode and the background E region where the vertical density gradient profile and the weaker than FB threshold ambient electric field were considered. From 2D density contour maps, it was found that the FB wave grows in the region of $\bar{N}_e \bar{E} > 0$ (where $\bar{N}_e$ is the electron density gradient and $\bar{E}$ is the electric field), the initial growth rate was in reasonable agreement with the prediction of the combined linear theory of Farley-Buneman and gradient drift instabilities, and the propagation speed was modulated by the gradient strength. According to the phase velocity evaluated by the Fourier analysis and peak to peak estimation method, the density gradients were found to have an effect of lowering the phase velocity at saturation, which is smaller than ion-acoustic speed for large scale waves, and the results demonstrated that the reduction of phase velocity by a density gradient effect was larger for a longer wavelength wave than shorter wavelength curve. It was also found that the plausible density gradient effects seem to be related to the thickness of the density gradient region and vertical electric field where the FB wave was traveling. The thicker unstable layer would cause a greater phase velocity reduction than the thinner unstable layer might cause, and the large driving electric field would reduce the wavelength dependence of density gradient effect on the saturation phase velocity.

Key words: Gradient effects, Farley-Buneman waves, E region

Citation: Fern, C. L. and F. S. Kuo, 2009: Numerical study of plasma density gradient effects on farley-buneman waves traveling in the equatorial E region. Terr. Atmos. Ocean. Sci., 20, 645-659, doi: 10.3319/TAO.2008.08.22.01(AA)

1. INTRODUCTION

The existence of plasma waves in the E region has been known for several decades. Numerous studies on those plasma waves have led to a conclusion that the mechanisms generating the plasma waves demonstrate Farley-Buneman (FB) and the gradient-drift (GD) instabilities (e.g., see Fejer and Kelley 1980; Farley 1985; Kelley 1989). If the driving-electric-field is strong enough, the FB instability will generate short-scale (at the order of meter or smaller) FB waves (called type 1 waves in the ionospheric physics literature) directly. If there is a density gradient along the direction perpendicular to the magnetic field (vertical gradients at the magnetic equator, horizontal gradients at high latitude), the region can become unstable for a much weaker

electric field via the GD instabilities and excite large-scale waves usually of wavelengths at the order of tens of meters or larger. The shorter wavelength waves seen by radar (type 2 waves) were proposed to be generated by a nonlinear cascade process (McDonald et al. 1974; Keskinen et al. 1979; Sudan 1983b; Farley 1985; Haldoupis et al. 2005).

Following the combined linear theory of Farley-Buneman and gradient-drift (FB-GD) instabilities, if the density gradients exist along the ambient electric field which is slightly weaker than the FB instability threshold electric field, the short-scale FB waves can still be excited directly. Because the threshold condition varies with the wavelength under the density gradient condition, Farley and Fejer (1975) attributed the type 1 spectrum broadening to the effect of the density gradient term of the FG-GD instability theory. The observation evidence of a density gradient effect

* Corresponding author
  E-mail: fengcl@yuntech.edu.tw

on type 1 waves was presented by Hanuise and Crochet (1981), who found the lower type 1 Doppler velocities as their radar observation shifted from higher to lower radar frequencies. They attributed the lower instability thresholds to a destabilized ambient plasma density gradient. It was also applied extensively in numerous studies such as the interpretations of types 3 and 4 VHF aurora echoes (e.g., see a review by Moorcroft 2002). In situ rocket measurements (Haldoupis et al. 2000, 2005) of E-region electron density profile had shown that the density gradients existed widely in any latitude E-region of 100 - 110 km altitude, and that the scale lengths of the destabilized plasma density gradient originated from sporadic E layer were smaller than 2 km. However, Haldoupis et al. (2005) argued against a density gradient effect on short-scale FB waves, because they found no gradient drift effects on lowering the FB instability threshold and the wavelength dependence of phase velocity by the observation of two radar frequencies at 144 and 50 MHz. They also pointed out that the other statistical HF radar studies in the aurora region (e.g., Hanuise et al. 1991; Milan et al. 1997; Milian and Lester 2001; Lacroix and Moorcroft 2001) had also reached the same conclusion. However, their studies had focused on the shorter scale FB waves of wavelengths of 1 and 3.15 m, and the relevant HF radar observations were located in the aurora region with a strong electric field, where some physical mechanisms are still not completely understood and clearly need more accurate study using more precise techniques including numerical simulation.

Several of 2D nonlinear simulations of short-scale FB waves have been performed respectively using a particle code (Janhunen 1994), hybrid code (Oppenheim and Otani 1996) and fluid code (Newman and Ott 1981; Fern et al. 2001). The 2D nonlinear simulations of large-scale GD instability were developed by McDonald et al. (1974); however, there is still no 2D nonlinear simulation on FB-GD theory, probably because it is difficult to combine the short-scale FB instability and large-scale GD instability, especially for particle code and hybrid code which needs extraordinarily large computer working space for large-scale range. In this paper, we extended the simulation of FB instability into large-scale range containing plasma density gradients by a 2D fluid code, and studied the possible gradient effects on FB waves. We found that the thickness of the vertical region and vertical electric field where horizontal FB waves were traveling are possible factors of the gradient effects on FB waves.

2. NUMERICAL MODEL FOR DENSITY GRADIENT EFFECTS ON FARLEY-BUNEMAN WAVES

2.1 Numerical Model and Method of Data Analysis

It is known that a density gradient distribution exists within large scale space, where the wavelength of two-stream waves (i.e., FB waves) about $1 \sim 30$ m would be re-

garded as small scale. The past 2D simulations of pure two-stream waves, such as particle code or hybrid code, focused only on a much smaller scale waves, so that the 2D simulation of density gradient effect on two-stream waves covering large scale space was practically non-existent. Pfaff et al. (1987) compared the growth rate of FB waves calculated by Schmidt and Gary (1973) with the spectrum of electric field fluctuations measured in the CONDOR rocket flight and found that, the fluid theory is accurate for FB waves with wavelength larger than 3 m, and the kinetic theory should be taken into consideration for the smaller scale waves with wavelength smaller than 2 m. Our numerical model is basically a fluid code, detailed in a previous paper (Fern et al. 2001). For the convenience of the readers, we put the numerical model in Appendix A. The numerical computations were performed on a two-dimensional Cartesian mesh using 81 points in the x direction (east-west) and 261 points in the z direction (vertical), where the length X of the simulation box in the x direction for matching small scale horizontal wave is far smaller than the length Z in the z direction corresponding to the large scale background space. A periodic boundary condition is imposed on both electron density n and electric potential   in both x- and z-direction, a symmetric electron density gradient distribution in the vertical z-direction (see the sketch in Fig. 1) matching the periodic boundary is superposed on the constant background. At $t = 0$, the electrons are set to move uniformly at drift velocity $\vec{V}_D$, and the ions assume a constant velocity $\vec{V}_{i0} = $ $_i\vec{E}_0/\nu_{in}B_0$, where $_i$ and ν_{in} are the ion-gyro frequency and ion-neutral collision frequency respectively, $\vec{E}_0$ is the background driving electric field and B_0 is the magnetic field strength. Then a density perturbation with amplitude δn $n_0 \sin(\ell x)$ is superposed on the background density, where ℓ is the wavenumber to be assigned. A complete simulation will produce a data set of perturbation density $\delta n(x, z, t)$ for analysis.

By a series of computations, the perturbation density $\delta n(x, z, t)$ at each grid point at every time step is obtained. In addition to plotting the 2D density contour maps at some simulation time step to reveal the 2D evolution of plasma density, the spatial-Fourier analysis of plasma density variation in the x-direction at a fixed height z and at time t (we sampled only the first time step of every 10 steps without loss of wave information) is also made to obtain the information of different wave modes,

$$\delta n(x, z, t) = \sum_k \left[A_k(z, t)\cos(kx) + B_k(z, t)\sin(kx) \right]$$

(1)

The horizontal wavelength with wave-number k is $2\pi/k$, which is well defined by the horizontal length X of our simulation box. For example, the wavelength of the 6th horizontal spatial Fourier mode is $X/6$, and so forth. Then the coeffi-
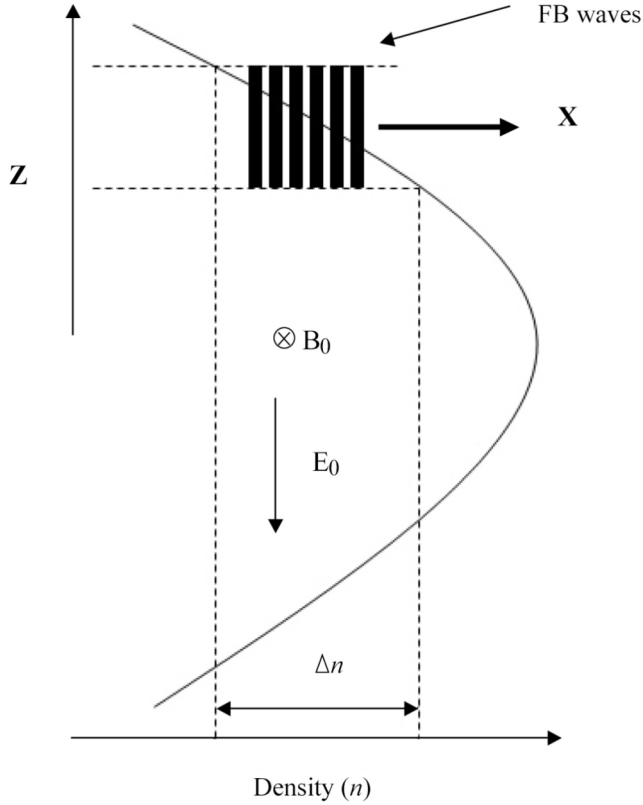
Fig. 1. The sketch graph for the limited vertical scale of horizontal FB wave covering vertical density variation Δn, where x representing horizontal direction, z representing vertical direction. The vertical electric field E_0 is directed downward and magnetic field B_0 directed inward.

cient $A_k(z, t)$ is plotted as function of time t, from which we may estimate the wave period of each wave by measuring the time interval between two successive peaks, hence the horizontal phase velocity can be determined. We may also identify each wave from the plots as a growing or damping wave, since the wave will neither grow nor dampen at the threshold and enable us to estimate the FB-GD instability threshold for the two-stream wave by a series of simulations at a different electron drift velocity. We may also evaluate the absolute amplitude $\sqrt{A_k^2 + B_k^2}$ of each wave at every time step and then calculate the linear growth rate by least square fitting method. The estimation of growth rate will help us estimate the FB-GD instability threshold.

2.2 A Test of the Numerical Model Using the Linear FB-GD Instability Theory

The linear instability theory of the ionospheric E-region plasma waves had been presented, discussed, and applied in numerous papers. The FB-GD instability mechanisms can account for density gradient effects on FB two-stream waves and be combined mathematically in the same dispersion relation, which was derived from the electron and ion equa-

tions of motion and continuity equation. For plasma waves propagating perpendicular to the magnetic field, the solution of the dispersion equation in the absence of neutral wind takes the familiar form associated with the plasma wave frequency ω and growth rate γ:

$$\omega = \frac{\vec{k} \cdot \vec{V}_d}{1 + \psi} \tag{2}$$

$$\gamma = \frac{\psi}{\nu_i (1 + \psi)} \left\{ \left[\left(\frac{\vec{k} \cdot \vec{V}_d}{1 + \psi} \right)^2 - k^2 C_s^2 \right] \right. $$
$$\left. + \frac{\nu_i \Omega_e \vec{k} \cdot \vec{V}_d}{\nu_e k (L_N)_\perp (1 + \psi)} \right\} - 2\alpha N_e \tag{3}$$

where $\psi = \nu_i \nu_e / \Omega_i \Omega_e$, ν_e, ν_i, Ω_e, and Ω_i are the electron-neutral collision frequency, ion-neutral collision frequency, electron gyro-frequency and ion gyro-frequency respectively, $\vec{k}$ is the plasma wave vector, C_s is the ion acoustic speed, N_e is the mean electron density and α is the recombination coefficient. $\vec{V}_d$ is the relative electron-ion drift velocity in windless situation and is approximately equal to the Hall drift velocity $\vec{V}_e \approx \vec{E} \times \vec{B} / B^2$, and $(L_N)_\perp = N_e / (\nabla N_e)$ is the scale length of electron density gradient perpendicular to B-field and parallel to E-field. $(L_N)_\perp$ is taken as positive if $(\nabla N_e) \cdot \vec{E} > 0$. Note that Eq. (3) is valid for $\nu_i > \omega \gg \gamma$, and that the stabilizing recombination term $2\alpha N_e$ is negligible for short-scale plasma waves which are of interest to E-region radio backscatter studies. Thus, the growth rate γ in a windless situation can be rewritten as follows:

$$\gamma = \frac{\psi}{\nu_i (1 + \psi)} \left\{ \underline{\left[\left(\frac{\vec{k} \cdot \vec{V}_e}{1 + \psi} \right)^2 - k^2 C_s^2 \right]}_{\text{(FB)}} \right.$$
$$\left. + \underline{\frac{\nu_i \Omega_e \vec{k} \cdot \vec{V}_e}{\nu_e k (L_N)_\perp (1 + \psi)}}_{\text{(GD)}} \right\} \tag{4}$$

where the underlined FB terms come from FB instability and the underlined GD term is responsible for GD instability. It can be seen from the above equation that an ambient electric field $\vec{E}$ and an electron density gradient ∇N_e constitute the agents that provide the free energy for destabilization of E-region plasma. Here, we will apply our 2D numerical model to cross-check with the linear FB-GD instability theory. First, we utilized the hyperbolic function to establish a symmetric electron density profile in the vertical z direction which is similar to a real layer structure, i.e.,

$$N_e(z) = N_0 \left\{ 1 + G \times \left[1 - \tanh^2 \left(\frac{z - z_{peak}}{\delta z} \right) \right] \right\} \qquad (5)$$

where z_{peak} represents the height of density peak, δz characterizes the possible scale size of vertical variation which controls the gradient shape, and G determines the value of the peak density. Figure 2 shows the density profile with $z_{peak} = 390$ m, $\delta z = 72$ m and $G = 0.08$ in a 2D simulated space of $X \quad Z = 30$ m $\quad 780$ m. The gradient scale length $L_z = N_e/(N_e / z)$ of the density distribution in Fig. 2 varies with altitude z. Figure 3a shows the gradient scale length L_z on the top half (390 ~ 780 m) of the symmetric density profile of Fig. 2. The region of the smaller gradient scale length which would yield larger GD effect is the focus of our subsequent analysis.

In order to study in detail the interaction between wave and vertical density gradient and the gradient-drift effects on two-stream waves, we introduced an 0.1% perturbation at each height [i.e., $\delta n = 0.001 N_0 \sin(kx)$] with single wave mode $k = 6$ corresponding to a horizontal wavelength of 5 m, and considered a weaker downward electric field $E_z = -11.2$ mV m^{-1} (corresponding to electron drift velocity $V_D = 400$ m s^{-1}) which is not large enough to trigger two-stream waves directly by FB instability alone. In other words, the excitation of a two-stream wave demands the contribution of
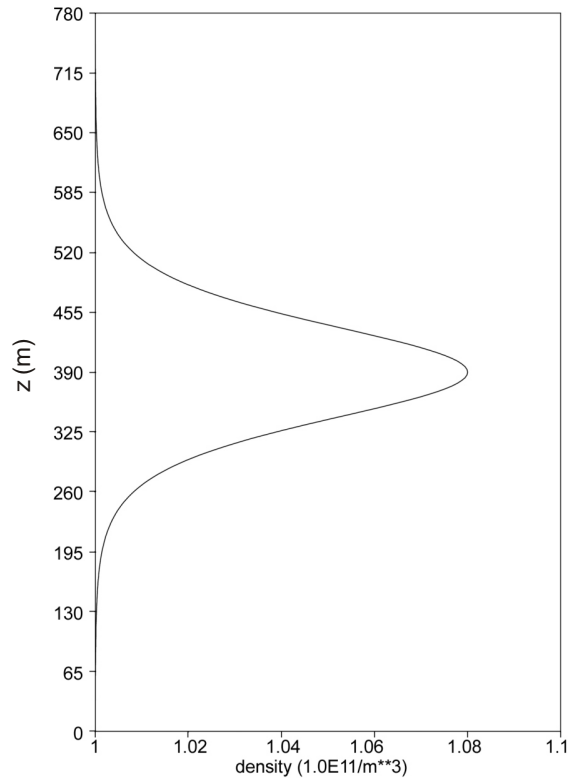
Fig. 2. The electron density distribution over height z obtained by Eq. (5) with $G = 0.08$, $\delta z = 72$ m, and $z_{peak} = 390$ m. This distribution is similar to a layer structure.
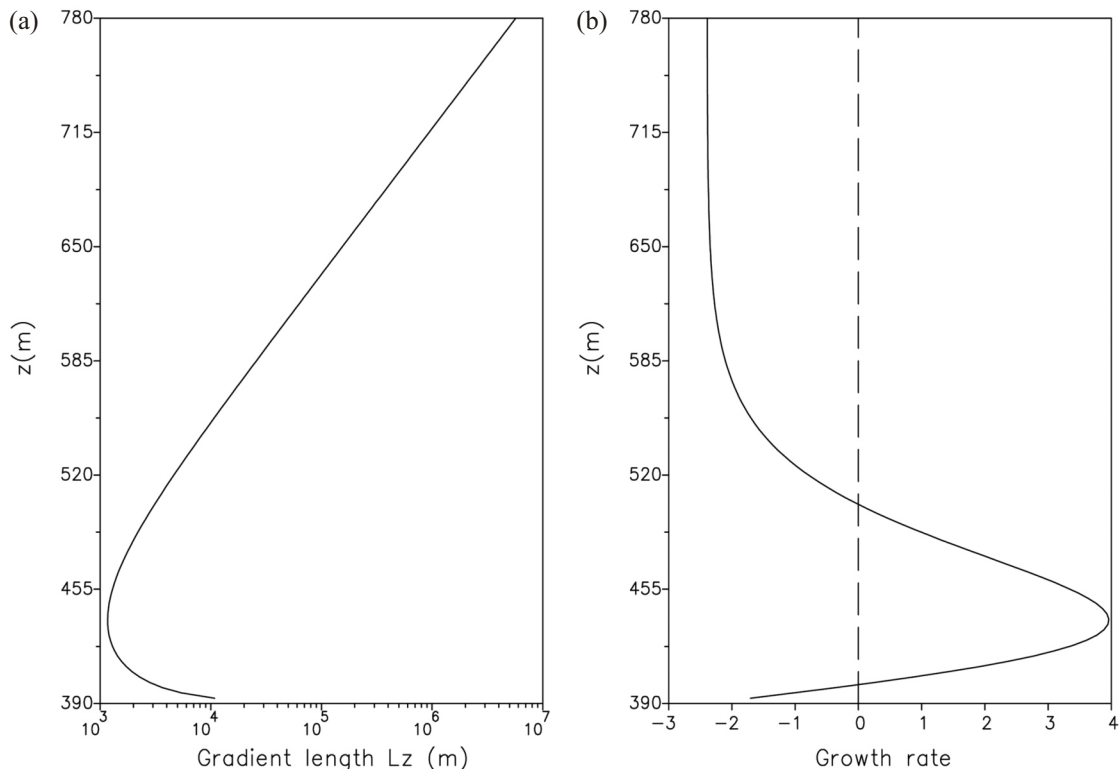
Fig. 3. (a) represents the height variation of the gradient scale length $L_z = N_e / | N_e|$ on the upper half of the density profile of Fig. 2 (i.e., 390 ~ 780 m) and (b) represents the corresponding height variation of theoretical growth rate derived from Eq. (4).

GD instability because the magnitude of polarization electric field is weaker than the threshold value $E_{th} = 12.2$ mV m^{-1} (corresponding to the threshold drift velocity $V_{Dth} = 437$ m s^{-1} obtained from $V_{Dth} = Cs(1 + \psi)$ and $Cs = 356$ m s^{-1}, $T_i = T_e = 230$ K). Other background parameters are listed in Table 1, where the magnetic field is perpendicular to the $x - z$ plane and the electric field is in a downward (vertical z) direction. Substituting all these simulation parameters into Eq. (4), we obtained the theoretical growth rate as a function of z as shown in Fig. 3b, where the region of bottom layer (0 ~ 390 m) is omitted due to $\bar{N}_e \cdot \vec{E} \approx 0$ (no GD instability). Judging from Fig. 3b, the evolution of plasma waves should be limited in the narrow region of the top layer at about 390 ~ 499 m where the growth rate is larger than zero. Meanwhile, 2D simulations of our numerical model yield a 2D gray scale map of density variation at different simulation time as shown in the top panel of Fig. 4, where the excited region of plasma waves is close to the theoretical prediction (see Fig. 3b), and the propagation speed varied with vertical position resulted from the different gradient scale length (L_z) at later time stage of simulation (see top-right panel of Fig. 4) from which we can find gradient-drift effects on phase velocities of FB waves predicted by FB-GD theory. Furthermore, the upward electric field $E_z = +11.2$ mV m^{-1} (i.e., $V_D = -400$ m s^{-1}) and a relatively weak downward electric field $E_z = -8.4$ mV m^{-1} (i.e., $V_D = 300$ m s^{-1}) were also studied. As a result, the upward electric field $E_z = +11.2$ mV m^{-1} will excite the plasma waves in the bottom layer as shown in the middle panels of Fig. 4 that still satisfy GD instability condition ($\bar{N}_e \cdot \vec{E} \le 0$), and the smaller downward electric field $E_z = -8.4$ mV m^{-1} will dampen plasma waves as shown in the bottom panel of Fig. 4 due to the larger negative value of FB term in Eq. (4). This result indicates that, regardless of the direction of electric field, GD instability can help excite FB waves at slightly smaller than FB instability threshold polarization electric field strength ($E_{th} = 12.2$ mV m^{-1}). From the above analysis, we see that our numerical model is qualitatively consistent with the linear FB-GD instability theory.

At the vertical position of maximum gradient $\bar{N}_e$, the plasma waves have the highest growth rate and can grow to saturation without being affected by the waves in the adjacent region where the gradient is weaker. So we picked the height $z = 438$ m (at the 147th height) where the gradient scale length is the smallest with $L_z \sim 1.2$ km and $\bar{N}_e \cdot \vec{E} \le 0$ to analyze the evolution of plasma wave. Fig. 5 displays the time variation of the primary 5 m wave at $z = 438$ m for different electron drift velocities derived from different downward electric fields. It can be found that the threshold drift velocity V_D is about 348 m s^{-1} and consistent with the prediction of FB-GD instability theory (see Fig. 6). Moreover, according to the time variation of wave amplitude shown in Fig. 5, the phase velocity can be evaluated in the initial growing stage by the peak-to-peak method. Table 2 listed the estimations of the phase velocities corresponding to differ-

ent drift velocities, where the threshold phase velocity V_p is about 273.49 m s^{-1} and the differences between simulation results and theoretical values were smaller than 3%. On the other hand, we can also fit the absolute amplitude of a 5 m wave in an early stage to find the linear growth rate by the least squares method. Figure 6a exhibits the estimates of linear growth for different electron drift velocities, where the closed circle represents simulation data and solid line represents theoretical estimation from Eq. (4) of FB-GD instability theory. Basically, the linear simulation data is in good agreement with the estimation of linear FB-GD theory.

2.3 The Behavior of a Longer Wavelength Wave

In order to study the behavior of a longer wavelength wave, we considered a 10m wave and extended horizontal space size from X to 60 m, that is, the simulation box size is $X \times Z = 60$ m $\times$ 780 m. Figure 7 shows the gray scale map of density variation for smaller electron drift velocity $V_D = 300$ m s^{-1} (i.e., $E_z = -8.4$ mV m^{-1}). It reveals that the 10 m wave receiving larger GD effects than 5 m wave can be excited by a smaller electric field by which 5 m wave can not be excited as shown in the bottom panel of Fig. 4. The estimations of growth rates for the 10 m wave with different electron drift velocities were shown in Fig. 6b, which were close to the theoretical values. The corresponding estimations of phase velocities were listed in Table 2, where the differences of 5 and 10 m waves for the same electron drift velocity in linear regime are very small and the phase velocity depends only on the electron drift velocity. This is in agreement with Eq. (2) for the linear FB-GD theory. From a series of qualitative analysis and quantitative estimation, it is confirmed that our numerical model is accurate for simulating FB-GD instability.

3. THE RESULT OF A SIMULATION IN A NONLINEAR STAGE

3.1 The Saturation Simulations Associated with Gradient Effect

FB-GD instability theory predicts that the phase velocity of FB wave in the presence of a density gradient effect does not depend on the scale size of the wave. This theory

Table 1. Parameters of the background condition.

Static magnetic field, $B_{0\hat{y}}$	0.28	G
Mean plasma density, N_0	1×10^{11}	m^{-3}
Temperature, T_e, T_i	230	K
Effective ion mass, m_i	5.0×10^{-26}	Kg
$e^- - n$ collision frequency, ν_{en}	4.0×10^4	s^{-1}
Ion-n, collision frequency ν_{in}	2.5×10^3	s^{-1}
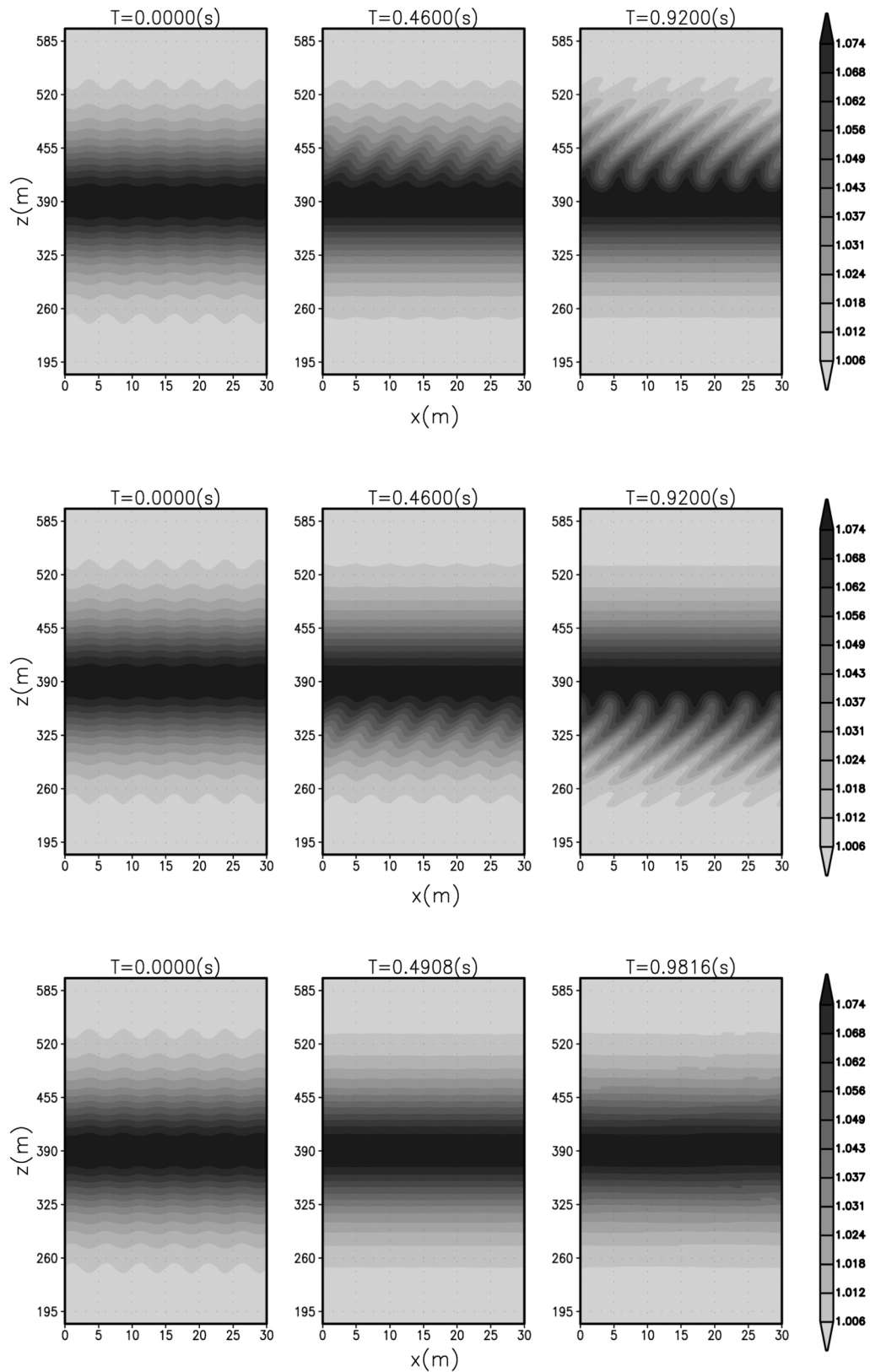
Fig. 4. The gray scale maps of density variation $n(x.z)$ for 5 m wave at different simulation time, where the **top panel** for downward electric field E_z = -11.2 mV m^{-1} (i.e., V_D = 400 m s^{-1}), the **middle panel** for upward electric field E_z = +11.2 mV m^{-1} (i.e., V_D = -400 m s^{-1}), and the **bottom panel** for downward electric field E_z = -8.4 mV m^{-1} (i.e., V_D = 300 m s^{-1}).
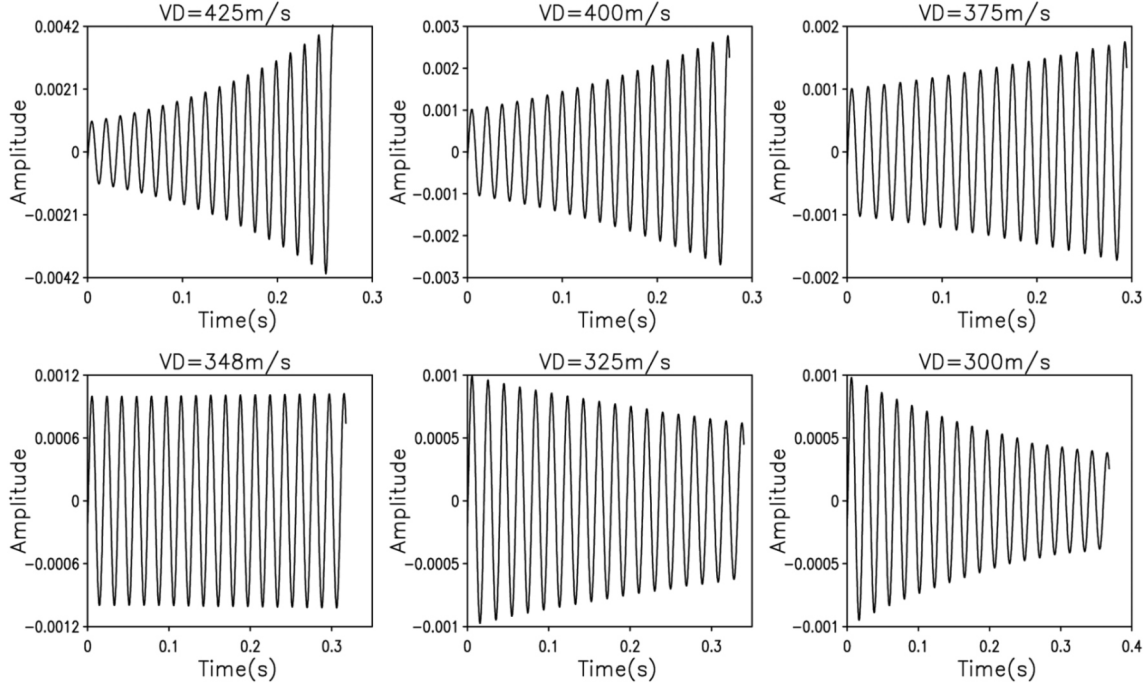
Fig. 5. Plots of the coefficient $A(z, t)$ of $\cos(kx)$ as a function of time t in the environment of different drift velocities, where z is the 147th height (i.e., $z = 438$ m) and $k = 1.256$ m^{-1} is the 6th horizontal Fourier mode (5 meter wave) in the X Z simulation box with $X = 30$ m and $Z = 780$ m.
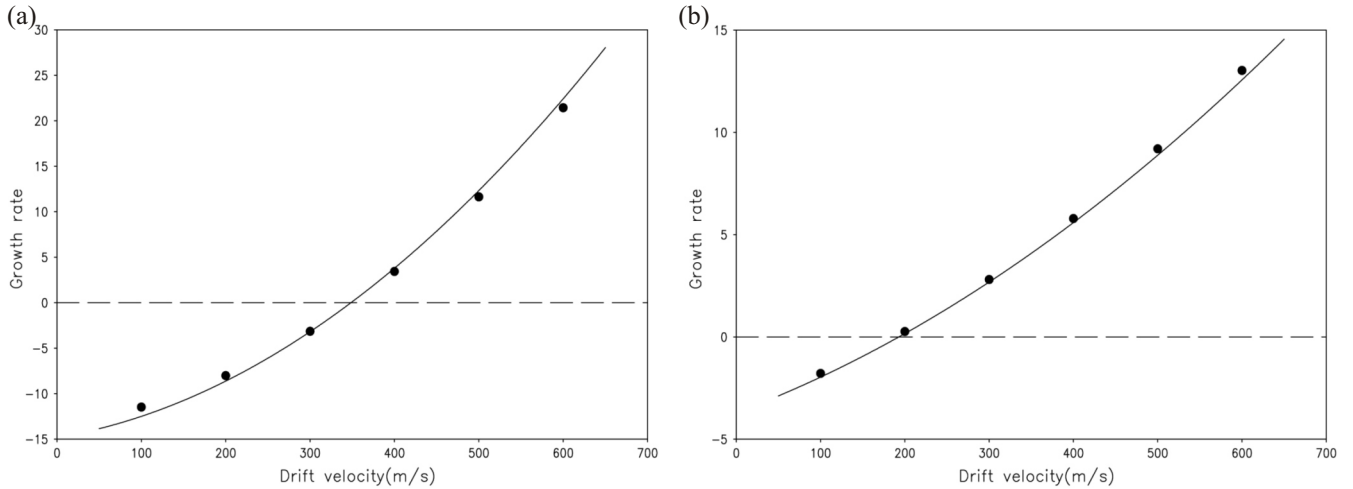
Fig. 6. The plots of the linear growth-rate of two-stream waves with respect to the electron drift velocity for 5 m wave (a) and 10 m wave (b), where the solid line represents the theoretical values obtained by Eq. (4) with $L_z = 1.2$ km, the closed circle represents the simulation results and the dash line represents the threshold value.

Table 2. Dependence of horizontal phase velocities V_p on drift velocity V_D [denoted by $V_p(V_D)$] of 5 meters wave and 10 meters wave obtained by numerical simulation on a 30 m × 780 m and 60 m × 780 m simulation box in different electron drift velocities V_D at fixed height $z = 438$ m corresponding to gradient scale length $L_z = 1.2$ km in linear regime, where the theoretical values were derived from Eq. (3) of linear FB-GD theory. The background density profile is given in Fig. 2. All velocities are in m s^{-1}.

	V_p (300)	V_p (325)	V_p (348)	V_p (375)	V_p (400)	V_p (425)	V_p (500)
Theoretical values	244.45	264.81	283.55	305.55	325.92	346.29	407.40
5 m wave	235.82	255.77	273.49	294.78	314.15	334.09	392.58
10 m wave	236.64	256.39	274.44	295.80	315.61	335.29	394.40
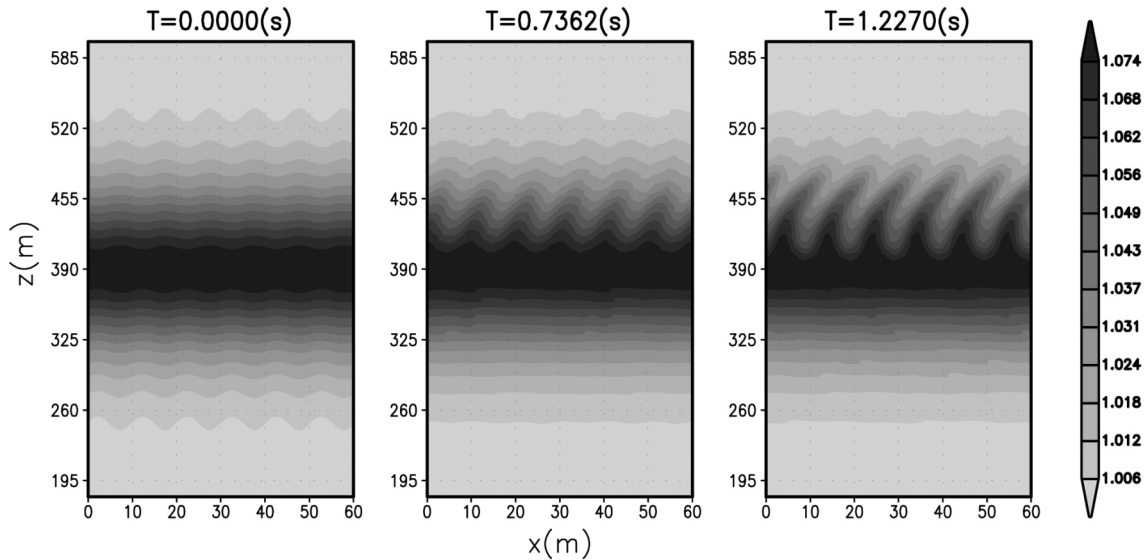
Fig. 7. The grey scale maps of density variation n(x, z) at a different simulation time, where the simulation started with 10 m wave perturbation and the electron drift velocity is V_D = 300 m s^{-1} (i.e., the downward electric field E_z = -8.4 mV m^{-1}).

has been confirmed by the simulation found in section 2.2; however, it is understood that the results of radar observations were most probably the result from the saturated two-stream waves. According to the saturation theory of two-stream waves, phase velocity in saturation regime will be close to the velocity of the marginally unstable wave corresponding to the threshold velocity of linear theory (e.g., Lee et al. 1974; Sudan 1983a, b; Hamza and St-Maurice 1993; Otani and Oppenheim 1998). Results of previous linear simulations with different electron drift velocities (Fig. 6) showed that, the different scale waves suffered from density gradient effect have different threshold. Nevertheless, in order to explore the possible saturation theory for density gradient effect, we will extend the analysis in the linear regime of previous section 2.2 into highly nonlinear stage and try to evaluate the phase velocity at saturation. Here it should be understood that a wave is said to be saturated if its energy gain equals to its energy loss in the nonlinear processes. Figure 8 shows the time evolutions of 5 , 10, and 15 m waves at z = 438 m corresponding to L_z ~ 1.2 km for the same electron drift velocity V_D = 400 m s^{-1} (i.e., E_z = -11.2 mV m^{-1}). It reveals that the waves ceased growing after maximum amplitude was reached, i.e., after entering the highly nonlinear stage and became saturated, and the maximum amplitude is larger for longer wavelength wave. From the gray scale map of density variation as shown in Fig. 9, we found that the primary waves with maximum amplitude are very prominent in the highly nonlinear stage, so we can apply the peak-to-peak method to evaluate the horizontal phase velocity of the primary waves at z = 438 m where the maximum gradient with L_z = 1.2 km was located. The relevant data was listed in Table 3.1, which clearly reveals that the phase velocities of different wavelength waves were approximately the same in

the linear regime, and became smaller in the saturated regime. The longer wavelength wave had a smaller phase velocity than the shorter wavelength wave in the saturated regime, which seems to be related to the maximum amplitude. The variations of phase velocities for different scale waves at saturation are consistent with the wavelength dependence of phase velocities resulted from density gradient effect.

Alternatively, we also made simulations for 5, 10, and 15 m waves over the same 2D space size of X Z = 90 m   780 m with fixed grid points of 241   261, leaving other background conditions (including the vertical density gradient distribution, V_D = 400 m s^{-1}, L_z = 1.2 km) unchanged. The results as listed in Table 3.2 were consistent with that of Table 3.1. Considering the resolution and computer resource in the following series of simulations, we shall adopt a variable horizontal space size with a fixed wave mode pegged at k = 6 for different waves and is the same resolution for different wavelength curve.

3.2 Simulations for Gradient Effects Related to 2D Structure of FB Waves

From the saturation simulations of section 3.1, we had demonstrated the wavelength dependence of phase velocity resulted from nonlinear processes. We also showed that the vertical density gradient distributions with different range and density peak can affect the variation of saturation phase velocity. As a matter of fact, the arguments for density gradient effects on two-stream waves were presented in a recent study (Haldoupis et al. 2005), so the exploration for the relations between gradient distribution and the wavelength dependence of phase velocity is worthwhile. Here, we considered three layers of density distribution derived from
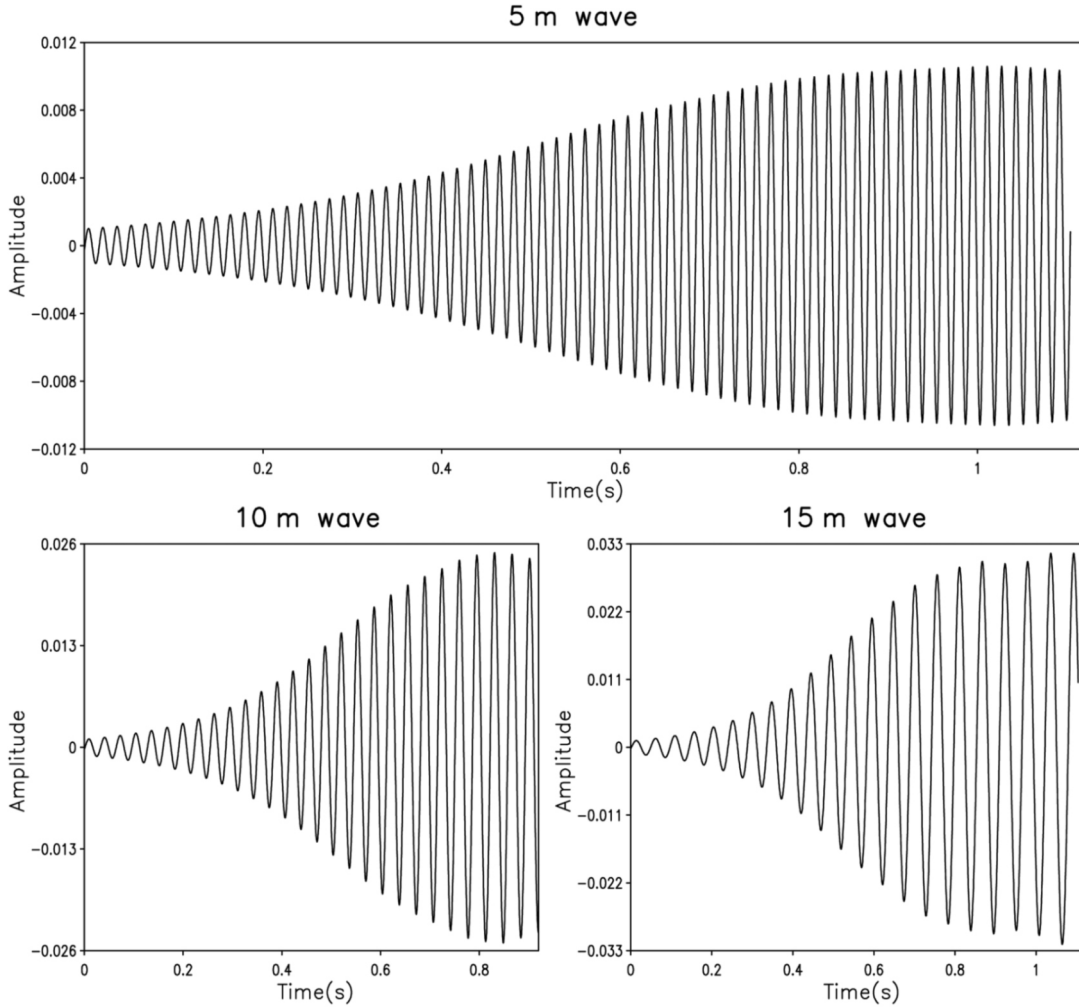
Fig. 8. The time variations of 5, 10, and 15 m waves at $z = 438$ m where the gradient length is $L_z = 1.2$ km and electron drift velocity is $V_D = 400$ m s^{-1} (i.e., the downward electric field $E_z = -11.2$ mV m^{-1}).
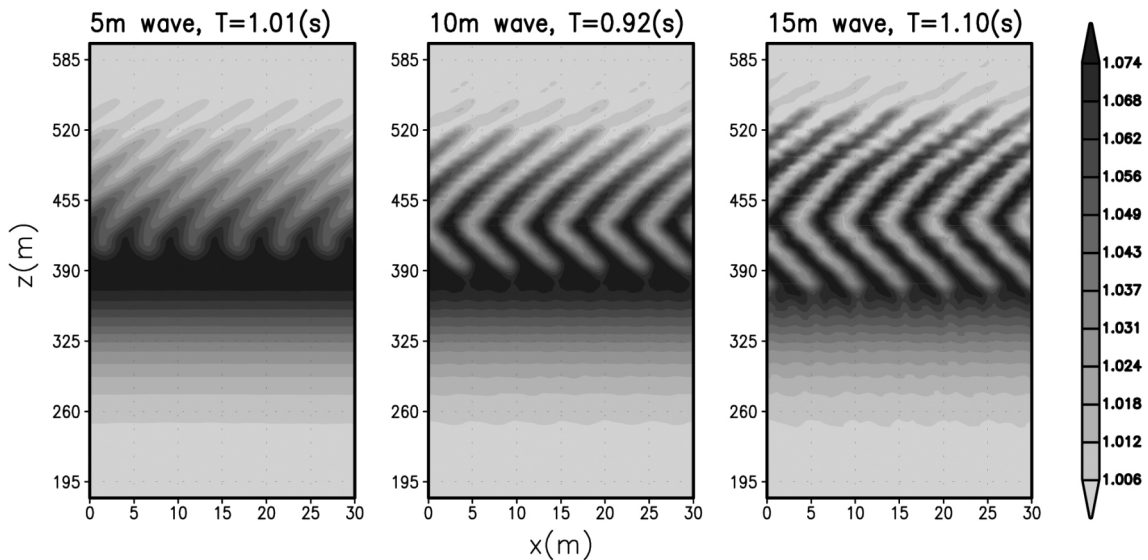
Fig. 9. The gray scale map of density variation $n(x, z)$ for different wave scale with same electron drift velocity $V_D = 400$ m s^{-1} (i.e., $E_z = -11.2$ mV m^{-1}) in the highly nonlinear stage, where the dimensions of 2D simulation space are 30 m × 780 m for 5 m wave, 60 m × 780 m for 10 m wave and 90 m × 780 m for 15 m wave respectively, but the grid points for three dimensions are 81 × 261 pts.

Table 3.1. The estimations of saturation phase velocities for a different wave scale with the same electron drift velocity V_D = 400 m s^{-1} (i.e., E_z = -11.2 mV m^{-1}) at some fixed height corresponding to the same gradient length L_z = 1.2 km, where the dimensions of 2D simulation space are 30 m × 780 m for 5 m wave, 60 m × 780 m for 10 m wave and 90 m × 780 m for 15 m wave respectively, but the number of grid points for each case is the same, i.e., 81 × 261 pts.

	5 m wave	10 m wave	15 m wave
Linear regime	314.15 m s^{-1}	315.61 m s^{-1}	315.06 m s^{-1}
Saturated regime	309.38 m s^{-1}	281.23 m s^{-1}	266.15 m s^{-1}

Table 3.2. The estimations of saturation phase velocities for a different wave scale with the same electron drift velocity V_D = 400 m s^{-1} (i.e., E_z = -11.2 mV m^{-1}) at some fixed height corresponding to the same gradient length L_z = 1.2 km, the simulations were made on the same 2D simulation space size of 90 m × 780 m with the same number of grid points 241 × 261 pts.

	5 m wave	10 m wave	15 m wave
Linear regime	317.82 m s^{-1}	316.63 m s^{-1}	316.34 m s^{-1}
Saturated regime	304.98 m s^{-1}	283.06 m s^{-1}	270.93 m s^{-1}

Eq. (5) as shown in Fig. 10, where case (C) has largest thickness, case (A) has smallest thickness and case (B) is between them, but their gradient variations are analogous. Two different horizontal waves (5 and 10 m wave) were studied using variable horizontal size X as described in section 3.1. Concurrently, the electron drift velocity V_D = 400 m s^{-1} (i.e., E_z = -11.2 mV m^{-1}) was assumed and the other background parameters remain the same as in Table 1. Figure 11 reveals the evolutions of 10 m waves at some fixed height [i.e., z = 414 m for case (A), z = 438 m for case (B), and z = 462 m for case (C)] corresponding to gradient scale length L_z = 1.2 km for the three different layers of Fig. 10. It also reveals in Fig. 11 that the maximum saturation amplitude increased with increasing density peak. The estimations of phase velocities for different wave scale at maximum saturation amplitude were listed on Table 4. It could be found that the wavelength dependence of phase velocities decreased with decreasing density peak of the layer.

From the grey scale maps of density variation at saturation of a 10 m wave for three different layers as shown in Fig. 12, we can see that the vertical scale of horizontal wave depends on the thickness of layers with different density peaks and means that the layers will limit the vertical evolution of 2D waves, where the layer with smaller density peak (representing smaller vertical density variation) such as case (A) corresponds to smaller vertical scale of 2D wave. Thus, through the above simulations and analysis, it is interesting that the vertical scale of 2D waves parallel to vertical density gradient will affect the horizontal wavelength dependence of phase velocities from GD effect. The result is possibly associated with the vertical density variation corresponding to vertical scale of 2D wave. In fact, the limited vertical scale of 2D waves in a large scale density gradient distribution also may cover the part of vertical density variations as shown in

the sketch of Fig. 1, so it can be expected that the wavelength dependence of phase velocities for small vertical scale waves will be unclear.
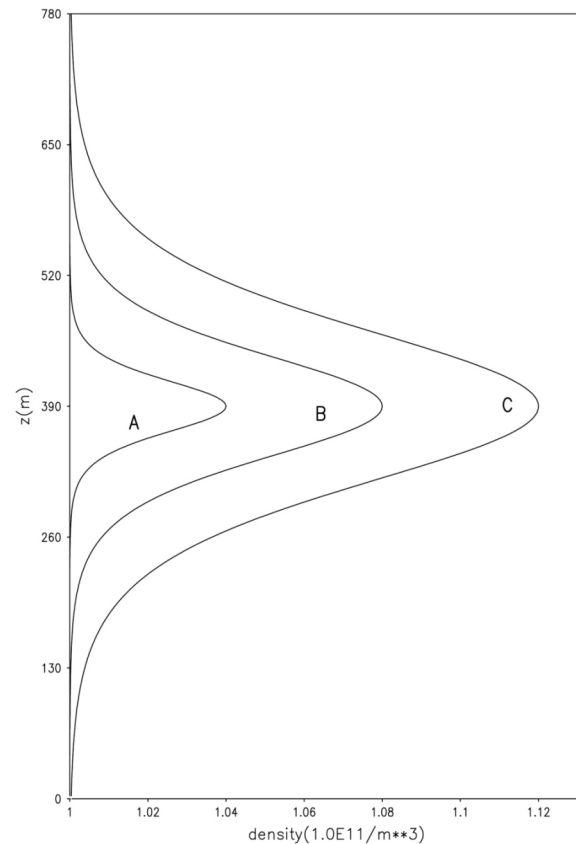
Fig. 10. Three density layer distributions with different peaks and analogous gradient variation derived from Eq. (5). Case (A): δz = 12 m and G = 0.04, case (B): δz = 24 m and G = 0.08, case (C): δz = 36 m and G = 0.12.
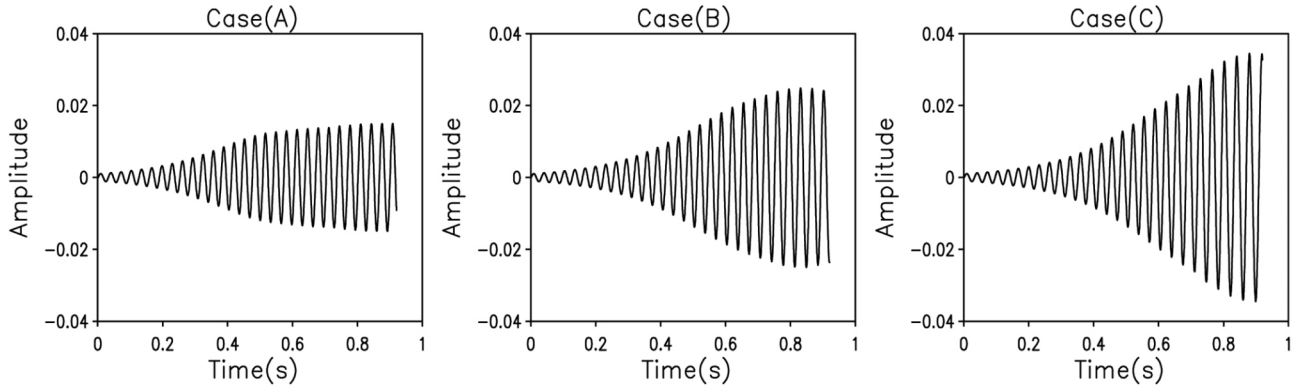
Fig. 11. The time variations of 10 m wave with electron drift velocity $V_D = 400$ m s^{-1} (i.e., $E_z = -11.2$ mV m^{-1}) at some fixed height corresponding to $L_z = 1.2$ km for three different density distributions.

Table 4. The estimations of saturation phase velocities of a different wave scale at the same electron drift velocity $V_D = 400$ m s^{-1} (i.e., $E_z = -11.2$ mV m^{-1}) for three different density layer distributions with different density peak and analogous gradient variation.

Wavelength	Case (A)	Case (B)	Case (C)
5 m	315.45 m s^{-1}	309.58 m s^{-1}	306.31 m s^{-1}
10 m	305.11 m s^{-1}	281.23 m s^{-1}	261.29 m s^{-1}
difference	10.34 m s^{-1}	28.35 m s^{-1}	45.02 m s^{-1}
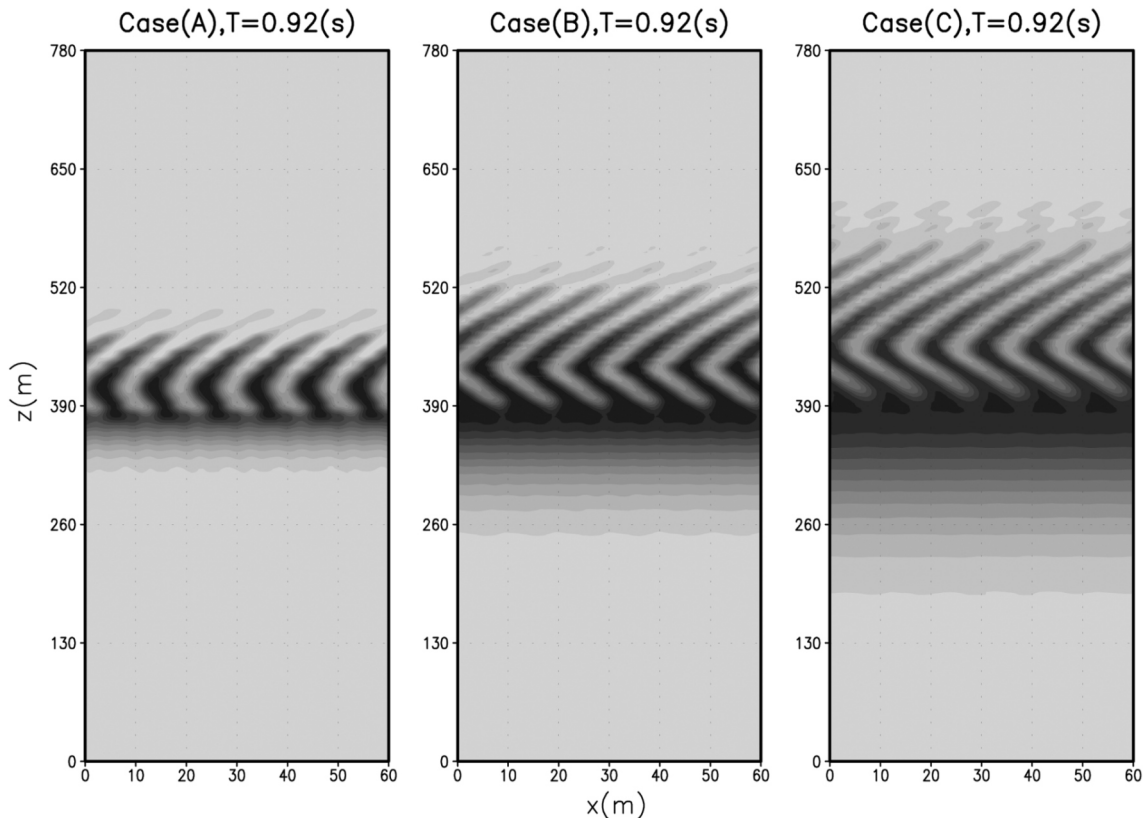
Fig. 12. The grey scale maps of density variation $n(x, z)$ in the highly nonlinear stage for three layers with different density peaks and analogous gradient variation. The simulation started with a 10 m wave perturbation and the electron drift velocity $V_D = 400$ m s^{-1} (i.e., $E_z = -11.2$ mV m^{-1}).

3.3 Simulations for Gradient Effect Related to Strong Electric Field

In order to emphasize GD effect in the previous simulations of sections 3.1 and 3.2, we considered the electron drift velocity $V_D = 400$ m s^{-1}, which is slightly smaller than the threshold value $V_{Dth} = 437$ m s^{-1} (i.e., $E_{th} = 12.2$ mV m^{-1}) of the FB instability. However, a strong electric field often appears in the equatorial electro-jet and polar region. Thus, we shall also study density gradient effect under the environment with large drift velocities which are larger than or near threshold value. In order to emphasize the prominent influence of FB instability we shall also consider a weaker density gradient distribution with its maximum gradient corresponding to a scale length $L_z = 6$ km at the location $z = 1437$ m (i.e., the 480th height). In order to investigate gradient effect on the wavelength dependence of phase velocities, three different wave lengths of 5, 10, and 15 m were studied by a 2D simulation with weak gradient layer distribution, where horizontal space size X is 6 times of the wavelength and vertical space size is $Z = 2.4$ km with total grid points of 81   801. Three electron drift velocities, namely, $V_D = 470$ m s^{-1} ($E_z = -13.16$ mV m^{-1}), $V_D = 450$ m s^{-1} ($E_z = -12.6$ mV m^{-1}) and $V_D = 430$ m s^{-1} ($E_z = -12.04$ mV m^{-1}) were considered leaving other background parameters unchanged. When the simulations of the waves reached maximum amplitude in the highly nonlinear stage, we used the previous methods of section 3.1 to analyze phase velocity of horizontal waves at fixed vertical position. Table 5 represents the estimations of phase velocities V_p of different scale waves for three drift velocities V_D at $z = 1437$ m. It was found that the differences among the saturation phase velocities of different scale waves decreased with increasing driving electric field (i.e., electron drift velocity). In other words, the wavelength dependence of the density gradient effect on phase velocities of different scale waves was weakened by increasing the driving electric field. Thus, we believe that the background electric field is an important factor for the reduction of gradient effect on FB waves.

4. SUMMARY AND DISCUSSION

We have carried out 2D simulations of density gradient effects on the phase velocity at saturation of two-stream waves. The simulations were focused on the pure interaction between single horizontal wave and a vertically symmetric electron density layer. The structure of the electron density layer defined by Eq. (5) is characterized by two parameters: G and δz. The ratio $G/\delta z$ determines the minimum gradient length (maximum growth rate of FB-GD instability) of the layer, and δz determines the thickness of the unstable layer. Our simulation results in the linear regime were consistent with the predictions of linear FB-GD instability theory, and confirmed the wavelength dependence of phase velocity in the saturated regime. However, our simulations also revealed that the vertical scale of 2D wave and vertical polarized electric field are possibly related to the wavelength dependence of phase velocity. The gradient scale length L_z is an important parameter in the linear theory of FB-GD instability, but the layer's thickness (characterized by δz) has gone unnoticed by the researchers. The results of this study clearly show that the thickness of the unstable layer has strong effect on the reduction of the phase velocity of FB wave on its way evolving from linear stage to saturation stage. The thicker unstable layer would cause more phase velocity reduction than the thinner unstable layer.

Since the evolutions of waves were limited in an unstable region, we can apply different density peak to find the possible relations between phase velocity at saturation and the thickness of the unstable layer. From the simulations found in sections 3.1 and 3.2, it was shown that the wave amplitude at saturation increased with increasing thickness of unstable layer, and the phase velocity at saturation decreased with increasing saturation amplitude. In general, the longer wavelength waves have larger saturation amplitude, because they have lower threshold therefore have larger unstable region to gain energy from background density gradient. However, if the density peak of a layer is small, that is, the unstable region is small, then the waves will obtain only small energy from background density gradient and saturation amplitude will also be reduced. Because a density layer has different gradient scale length at different height, the waves with weaker electric field will be limited in the larger density gradient region of the layer. So the density peak of the layer with vertical density variation is closely related to the vertical propagating range of waves which can represent the ver-

Table 5. The estimations of phase velocity dependence on electron drift velocity $V_p(V_D)$ for a different wave scale at saturation for the strong electric fields (i.e., the larger electron drift velocities) and a large scale density layer distribution with weaker gradient variation. All velocities are in m s^{-1}.

wavelength	$V_p(430)$	$V_p(450)$	$V_p(470)$
5 m	336.64	337.48	341.06
10 m	323.29	325.23	338.84
15 m	302.70	312.95	321.15

tical scale of 2D waves. In other words, the smaller density peak will result in a weaker gradient effect on FB waves. Similarly, we believe that the vertical range of FB waves will be limited in the E-region, because the complex environment including electric field variation, neutral wind, collision frequency variation and density gradient can affect the generation of FB waves. Thus, based on the possible limited vertical scale of 2D waves, we believe that the weaker gradient effect on FB wave will be found in the E region. However, radar observations only present 1D information of FB waves, and our 2D simulations can account for the relations between 2D property of FB waves and density gradient effect.

In addition, the strong electric field E will also reduce density gradient effect because the predominant FB instability tends to cause different wave scales reaching approximately the same phase velocity. Section 3.3 had demonstrated that the wavelength dependence of phase velocity from GD effect is unclear. Haldoupis et al. (2005) indicated that the past observations of HF and VHF aurora radar (e.g., Hanuise el al. 1991; Haldoupis et al. 2000; Lacroix and Moorcroft 2001) could not find GD effect on FB waves, but neglected a point that the very strong polarized electric field might exist in aurora region. The past studies of radar observations (e.g., St.-Maurice et al. 1986; Ravindran and Reddy 1993; Nielsen et al. 2002) also indicated that the large electron drift velocity derived from strong electric field would heat plasma and create larger phase velocity. Thus, the lower phase velocity derived from GD effect may be raised by the large electron drift velocity, so that the lower phase velocity which is lower than nominal ion acoustic speed (~ 360 m s^{-1}) is not easily found. In other words, the reduction of GD effect on FB waves, including the wavelength dependence of phase velocity and the lower phase velocity, can be explained by the existence of a strong vertical electric field.

In sum, our 2D simulations with a symmetric density layer were consistent with the linear FB-GD theory, so we can examine density gradient effects on FB waves. We have demonstrated, by the simulation of a single wave, that the vertical density variation involving 2D property of FB waves and polarized electric field will affect the display of density gradient effect on FB waves. Of course, the E-region ionosphere contains the interaction of multiple waves and the other parameters varying with vertical height, such as neutral wind, electric field, collision frequency, plasma temperature and so on. One advantage of numerical simulation is that, one can always isolate a specific factor from all the others by numerical simulation but not by radar experiment. Our simulations can clarify possible factors from complex environment variables. This paper suggests that the information of 2D wave scale and electric field variation is important in the study of density gradient effects on FB waves such that more observation data of other variables associated with density gradient effect is needed in the future.

REFERENCES

Boris, J. P. and D. L. Book, 1973: Flux-corrected transport. 1. SHASTA, a fluid transport algorithm that works. *J. Comput. Phys.*, **11**, 38-69, doi: 10.1016/0021-9991(73)90147-2. [Link]

Chou, S. Y. and F. S. Kuo, 1996: A numerical study of the wind field effect on the growth and observability of equatorial spread F. *J. Geophys. Res.*, **101**, 17137-17149, doi: 10.1029/96JA01404. [Link]

Farley, D. T., 1985: Theorey of equatorial electrojet waves: New developments and current status. *J. Atmos. Terr. Phys.*, **47**, 729-744, doi: 10.1016/0021-9169(85)90050-9. [Link]

Farley, D. T. and B. G. Fejer, 1975: The effect of the gradient drift term on type 1 electroject irregularities. *J. Geophys. Res.*, **80**, 3087-3090, doi: 10.1029/JA080i022p03087. [Link]

Fejer, B. G. and M. C. Kelley, 1980: Inonspheric irregularities. *Rev. Geophys.*, **18**, 401-454, doi: 10.1029/RG018i002p00401. [Link]

Fern, C. L., S. Y. Chou, and F. S. Kuo, 2001: Simulations of spectral asymmetries of pure two-stream waves in the equatorial electrojet. *Chin. J. Phys.*, **39**, 141-162.

Haldoupis, C., K. Schlegel, and G. C. Hussey, 2000: Auroral *E*-region electron density gradients measured with EISCAT. *Ann. Geophys.*, **18**, 1172-1181, doi: 10.1007/s00585-000-1172-x. [Link]

Haldoupis, C., T. Ogawa, K. Schlegel, J. A. Koehler, and T. Ono, 2005: Is there a plasma density gradient role on the generation of short-scale Farley-Buneman waves? *Ann. Geophys.*, **23**, 3323-3337. [Link]

Hamza, A. M. and J. P. St-Maurice, 1993: A turbulent theoretical framework for the study of current-driven E region irregularities at high latitudes: Basic derivation and application to gradient-free situations. *J. Geophys. Res.*, **98**, 11587-11599, doi: 10.1029/92JA02836. [Link]

Hanuise, C. and M. Crochet, 1981: 5-50-m wavelength plasma instabilities in the equatorial electrojet, 2. Thwo-stream conditions. *J. Geophys. Res.*, **86**, 3567-3572, doi: 10.1029/JA086iA05p03567. [Link]

Hanuise, C., J. P. Villain, J. C. Cerisier, C. Senior, J. M. Ruohoniem, R. A. Greenwald, and K. B. Baker, 1991: Statisical study of high-latitude E region Doppler spectra obtained with the SHERPA HF radar. *Ann. Geophys.*, **9**, 273-285. [Link]

Janhunen, P., 1994: Perpendicular particle simulation of the *E* region Fairly-Buneman instability. *J. Geophys. Res.*, **99**, 11461-11473, doi: 10.1029/94JA00206. [Link]

Kelley, M. C., 1989: The Earth's Ionosphere: Plasma Physics and Electrodynamics, Vol. 43, Academic Press, San Diego.

Keskinen, M. J., R. N. Sudan, and R. L. Ferch, 1979: Temporal and spatial power spectrum studies of numerical simulations of type II gradient drift irregularities in equatorial electrojet. *J. Geophys. Res.*, **84**, 1419-1430, doi: 10.1029/JA084iA04p01419. [Link]

Lacroix, P. J. and D. R. Moorcroft, 2001: Ion acoustic HF radar echoes at high latitudes and far ranges. *J. Geophys. Res.*, **106**, 29091-29103, doi: 10.1029/2001JA000024. [Link]

Lee, K., C. F. Kennel, and F. V. Coroniti, 1974: On the marginally stable saturation spectrum of unstable type I equatorial electrojet irregularities. *J. Geophys. Res.*, **79**, 249-266, doi: 10.1029/JA079i001p00249. [Link]

McDonald, B. E., T. P. Coffey, S. Ossakow, and R. N. Sudan, 1974: Preliminary report of numerical simulation of type 2 irregularities in the equatorial electrojet. *J. Geophys. Res.*, **79**, 2551-2554, doi: 10.1029/JA079i016p02551. [Link]

Milan, S. E. and M. Lester, 2001: A classification of spectral populations observed in HF radar backscatter from the E region auroral electrojets. *Ann. Geophys.*, **19**, 189-204.

Milan, S. E., T. K. Yeoman, M. Lester, E. C. Thomas, and T. B. Jones, 1997: Initial backscatter occurrence statistics from the CUTLASS HF radars. *Ann. Geophys.*, **15**, 703-718, doi: 10.1007/s00585-997-0703-0. [Link]

Moorcroft, D. R., 2002: Outstanding issues in the theory of radar aurora: Evidence from the frequency dependence of spectral characterictics. *J. Geophys. Res.*, **107**, 1301, doi: 10.1029/2001JA009218. [Link]

Newman, A. L. and E. Ott, 1981: Nonlinear simulations of type I irregularities in the equatorial electrojet. *J. Geophys. Res.*, **86**, 6879-6891, doi: 10.1029/JA086iA08p06879. [Link]

Nielsen, E., C. F. del Pozo, and P. J. S. Williams, 2002: VHF coherent radar signals from the E region ionosphere and the relationship to electron drift velocity and ion acoustic velocity. *J. Geophys. Res.*, **107**, doi: 10.1029/2001JA 900111. [Link]

Oppenheim, M. and N. Otani, 1996: Spectral characteristics of the Farley-Buneman instability: Simulations versus observations. *J. Geophys. Res.*, **101**, 24573-24582, doi: 10.1029/96JA02237. [Link]

Otani, N. F. and M. Oppenheim, 1998: A saturation mechanism for the Farley-Buneman instability. *Geophys. Res. Lett.*, **25**, 1833-1836, doi: 10.1029/98GL50868. [Link]

Pfaff, R. F., M. C. Kelley, E. Kudeki, B. G. Fejer, and K. D. Baker, 1987: Electric field and Plasma density measurements in the strongly-driven daytime equatorial electrojet, 2. Two-stream waves. *J. Geophys. Res.*, **92**, 13597-13612, doi: 10.1029/JA092iA12p13597. [Link]

Ravindran, S. and C. A. Reddy, 1993: Variation of type I plasma wave phase velocity with electron drift velocity in the equatorial electrojet. *J. Geophys. Res.*, **98**, 21581-21591, doi: 10.1029/93JA01051. [Link]

Schmidt, M. J. and S. P. Gray, 1973: Density gradients and the Fairly-Buneman instability. *J. Geophys. Res.*, **78**, 8261-8265, doi: 10.1029/JA078i034p08261. [Link]

St-Maurice, J. P., C. Hanuise, and E. Kudeki, 1986: On the dependence of the phase velocity of equatorial irregularities on the polarization electric field and theoretical implications. *J. Geophys. Res.*, **91**, 13493-13505, doi: 10.1029/JA091iA12p13493. [Link]

Sudan, R. N., 1983a: Unified theory of type I and type II irregularities in the equatorial electrojet. *J. Geophys. Res.*, **88**, 4853-4860, doi: 10.1029/JA088iA06p04853. [Link]

Sudan, R. N., 1983b: Nonlinear theory of type I irregularites in the equatorial electrojet. *Geophys. Res. Lett.*, **10**, 983-986, doi: 10.1029/GL010i010p00983. [Link]

Zalesak, S. T., 1979: Fully multidimensional flux-corrected transport algorithms to fluids. *J. Comput. Phys.*, **31**, 335-362, doi: 10.1016/0021-9991(79)90051-2. [Link]

APPENDIX A: NUMERICAL MODEL OF SIMULATION

Our numerical model was described in a previous paper (Fern et al. 2001). The *x*-axis of the rectangular coordinate system points to the east, the *y*-axis points to the north and the *z*-axis points upward. The governing equations consist of the continuity equation of plasma,

$$\frac{\partial n}{\partial t} + \nabla \cdot \left(n\vec{V}_e \right) = 0 \tag{A1}$$

the electron and ion velocity equations,

$$\vec{v}_e = \frac{\left(\frac{\Omega_e}{v_{en}}\right)^2 \left(\frac{\vec{E}'}{B_0} + \frac{K_B T_e}{eB_0} \frac{\vec{\nabla} n}{n} + \frac{v_{en}}{\Omega_e} \vec{V}_D \right) \times \frac{\vec{B}}{B_0}}{1 + \left(\frac{\Omega_e}{v_{en}}\right)^2} -$$

$$\frac{\frac{\Omega_e}{v_{en}}\left(\frac{\vec{E}'}{B_0} + \frac{K_B T_e}{eB_0} \frac{\vec{\nabla} n}{n} + \frac{v_{en}}{\Omega_e}\vec{V}_D \right)}{1 + \left(\frac{\Omega_e}{v_{en}}\right)^2} \tag{A2}$$

$$\frac{\partial \vec{v}_i}{\partial t} = -\frac{K_B T_i}{m_i} \frac{\vec{\nabla} n}{n} + \Omega_i\left(\frac{\vec{E}' + \vec{E}_0}{B_0} + \vec{v}_i \times \frac{\vec{B}}{B_0} \right)$$
$$- v_{in}\vec{v}_i - \left(\vec{v}_i \cdot \vec{\nabla} \right)\vec{v}_i \tag{A3}$$

and the equation for quasi-neutrality condition,

$$\vec{\nabla} \cdot \vec{J} = 0 \tag{A4}$$

where $\vec{J}$ $ne(\vec{V}_i$ $\vec{V}_e)$ $ne(\vec{v}_i$ $\vec{V}_D$ $\vec{v}_e)$ is the current density and *n* is the number density of the plasma; K_B is the

Boltzmann constant; $\nu_{in}, \nu_{en}, \kappa_i, \kappa_e, T_i, T_e, \vec{B}, \vec{E}, \vec{V}_D, \vec{v}_e$, and $\vec{v}_i$ are the ion-neutral collision frequency, the electron-neutral collision frequency, ion gyro-frequency, electron gyro-frequency, ion temperature, electron temperature, magnetic field, perturbation electric field, mean flow electron drift velocity, perturbation electron and ion velocity respectively; $\vec{V}_i$ and $\vec{V}_e$ can be taken as $\vec{V}_i = \vec{v}_i$; $\vec{V}_e = \vec{V}_D + \vec{v}_e$. Substituting all these physical quantities into Eq. (A4), we obtain Eq. (A5):

$$\nabla^2 \Phi + \frac{\partial \Phi}{\partial x}\left(\frac{\partial n/\partial x}{n} - \kappa_e \frac{\partial n/\partial z}{n}\right) + \frac{\partial \Phi}{\partial z}\left(\kappa_e \frac{\partial n/\partial x}{n} + \frac{\partial n/\partial z}{z}\right)$$

$$= \frac{K_B T_e}{e}\left(\frac{\partial^2 n/\partial x^2}{n} + \frac{\partial^2 n/\partial z^2}{n}\right) - B_0 V_D \left(\kappa_e \frac{\partial n/\partial x}{n} + \frac{\partial n/\partial z}{n}\right)$$

$$+ \left(\frac{1}{\kappa_e} + \kappa_e\right) B_0 \left(\frac{\partial n/\partial x}{n} v_{ix} + \frac{\partial n/\partial z}{z} v_{iz} + \frac{\partial v_{ix}}{\partial x} + \frac{\partial v_{iz}}{\partial z}\right)$$

$$(A5)$$

where $\Phi(x, z)$ is the potential function for the perturbed electric field $\vec{E}$, i.e., $\vec{E} = -\nabla \Phi$.

The eastward mean flow drift velocity $\vec{V}_D$ of the electrons is driven by a vertically downward zero order polarization electric field $\vec{E}_0 = \vec{V}_D \times \vec{B}_0$, where $\vec{B} = B_0 \hat{e}_y$ is a constant magnetic field B_0 of 0.28 G pointing to the north. The ion-neutral collision frequency ν_{in} and electron-neutral collision frequency ν_{en} are assumed to be constant in our simulation range with $\nu_{in} = 2.5 \times 10^3$ s^{-1} and $\nu_{en} = 4.0 \times 10^4$ s^{-1}. The ion and electron temperatures are assumed to be 230 K. The background plasma can be regarded as uniform with number density of 1.0×10^{11} m^{-3}. These background parameters are similar to that used in the past studies of equatorial electrojet (McDonald et al. 1974).

The numerical computations were performed on two-dimensional Cartesian mesh using 81 points in the x direction (east-west) and 261 points in the z direction (vertical). Periodic boundary condition is imposed on both electron density n and electric potential Φ in the x and z direction. Flux-corrected transport (FCT) technique (e.g., Boris and Book 1973; Zalesak et al. 1979) has been applied to carry out the time integration of the continuity Eq. (1). A detailed discussion of the application of FCT technique to study ionospheric irregularities can be referred to (Chou and Kuo 1996). At $t = 0$, the electrons are set to move uniformly at drift speed $\vec{V}_D$, and the ions assume a constant velocity $\vec{V}_{i0} = \kappa_i \vec{E}_0 / \nu_{in} B_0$, which is the steady state velocity of ions under the combined force from electric field $\vec{E}_0$ and the ion-neutral collision (note that $\nu_{in} \gg \kappa_i$). Then a density perturbation with amplitude $\delta n = n_0 \sin(kx)$ is superposed on the background density N_0, where k is the wave-number to be assigned. At each time step of computation, the electron velocity at each grid point is calculated from Eq. (A2), and the ion velocity at each grid is obtained by solving the differential Eq. (A3) using 2nd order Runge-Kutta scheme. These velocities and densities at each grid are substituted into Eq. (A5) to solve for the electric potential $\Phi(x, z)$ using the successive-over-relaxation (SOR) technique. Then, the plasma density distribution $n(x, z)$ at time $t + \Delta t$ is calculated by the FCT scheme to complete one cycle of the computation. In order to guarantee the numerical accuracy, we set the absolute error limit in the potential solver as small as 10^{-4}. The simulation is called to stop whenever the relative error of any grid fails to converge to within this error limit within 10000 steps of SOR iteration. This criterion sets a limit for density gradient, beyond which the off-diagonal terms become so much larger than the diagonal terms in Eq. (A5) that the SOR calculation fails to converge. That means that, the simulation will be stopped when the density gradient becomes so sharp that the small waves with scale-length comparable to the grid size starts to grow.